Arteaga Sierra, FR.; Milián Enrique, C.; Torres-Gómez, I.; Torres-Cisneros, M.; Moltó, G.; Ferrando Cogollos, A. (2014). Supercontinuum optimization for dual-soliton based light sources using genetic algorithms in a grid platform. Optics Express. 22(19):23686-23693. doi:10.1364/OE.22.023686.

Supercontinuum optimization for dual-soliton based light sources using genetic algorithms in a Grid platform

F. R. Arteaga-Sierra,[1,2,*] **C. Milián,**[2,3,6] **I. Torres-Gómez,**[1] **M. Torres-Cisneros,**[4] **G. Moltó,**[3] **and A. Ferrando**[2,5]

[1] *Centro de Investigaciones en Óptica, A.C., León Gto. 37150, México*
[2] *Universidad Politécnica de Valencia, Grupo de Modelización Multidisciplinar Intertech, 46022, Valencia, Spain*
[3] *Instituto de Instrumentación para Imagen Molecular (I3M). Centro mixto CSIC-Universitat Politècnica de València-CIEMAT, camino de Vera s/n, 46022 Valencia, España*
[4] *NanoBioPhotonics Group, DICIS, Universidad de Guanajuato, Mexico*
[5] *Departament d'Òptica, Universitat de València, Burjassot (València). 46100, Spain*
[6] *Current address: Centre de Physique Théorique, École Polytechnique, CNRS, F-91128 Palaiseau, France*
**arteaga@cio.mx*

Abstract: We present a numerical strategy to design fiber based dual pulse light sources exhibiting two predefined spectral peaks in the anomalous group velocity dispersion regime. The frequency conversion is based on the soliton fission and soliton self-frequency shift occurring during supercontinuum generation. The optimization process is carried out by a genetic algorithm that provides the optimum input pulse parameters: wavelength, temporal width and peak power. This algorithm is implemented in a Grid platform in order to take advantage of distributed computing. These results are useful for optical coherence tomography applications where bell-shaped pulses located in the second near-infrared window are needed.

OCIS codes: (190.4370) Nonlinear optics; (060.5530) Pulse propagation and temporal solitons; (230.6080) Sources; (110.2945) Illumination design; (170.4500) Optical coherence tomography.

References and links

1. J. P. Gordon, "Theory of the soliton self-frequency shift," Opt. Lett. **11,** 662–664 (1986).
2. F. M. Mitschke and L. F. Mollenauer, "Discovery of the soliton self-frequency shift," Opt. Lett. **11,** 659–661 (1986).
3. J. M. Dudley, G. Genty and S. Coen, "Supercontinuum generation in photonic cristal fibers," Rev. Mod. Phys. **78,** 135–1184 (2006).
4. D. V. Skryabin and A. V. Gorbach, "Colloquium: looking at a soliton through the prism of optical supercontinuum," Rev. Mod. Phys. **82,** 1287–1299 (2010).
5. A. V. Gorbach and D. V. Skryabin, "Light trapping in gravity-like potentials and expansion of supercontinuum spectra in photonic-crystal fibres," Nat. Photon. **1,** 1749-4885 (2007).
6. A. Hause, T. X. Tran, F. Biancalana, A. Podlipensky, P. St.J. Russell and F. Mitschke, "Understanding Raman-shifting multipeak states in photonic crystal fibers: two convergent approaches," Opt. Lett. **35,** 2167–2169 (2010).
7. A. Hause and F. Mitschke, "Soliton trains in motion," Phys. Rev. A **82,** 043838 (2010).
8. T. X. Tran, A. Podlipensky, P. St. J. Russell and F. Biancalana, "Theory of Raman multipeak states in solid-core photonic crystal fibers," J. Opt. Soc. Am. B **27,** 1785–1791 (2010).
9. Andrey V. Gorbach and Dmitry V. Skryabin, "Soliton self-frequency shift, non-solitonic radiation and self-induced transparency in air-core fibers," Opt. Express **16,** 4858–4865 (2008).

10. C. Milián, D. V. Skryabin and A. Ferrando, "Continuum generation by dark solitons," Opt. Lett. **34,** 2096–2098 (2009).
11. C. Milián, A. Ferrando, and D. V. Skryabin, "Polychromatic Cherenkov radiation and supercontinuum in tapered optical fibers," J. Opt. Soc. Am. B **29,** 589-593 (2012).
12. F. R. Arteaga-Sierra, C. Milián, I. Torres-Gómez, M. Torres-Cisneros, A. Ferrando, and A. Dávila, "Multi-peak-spectra generation with Cherenkov radiation in a non-uniform single mode fiber," Opt. Express **22,** 2451-2458 (2014).
13. S. A. Dekker, A. C. Judge, R. Pant, I. Gris-Sánchez, J. C. Knight, C. M. De Sterke and B. J. Eggleton, "Highly-efficient, octave spanning soliton self-frequency shift using a specialized photonic crystal fiber with low OH loss," Opt. Express **18,** 17766–17773 (2011).
14. J. Rothhardt, A. M. Heidt, S. Hädrich, S. Demmler, J. Limpert and A. Tünnermann, "High stability soliton frequency-shifting mechanisms for laser synchronization applications," J. Opt. Soc. Am. B **29,** 1257–1262 (2012).
15. A. M. Al-kadry and M. Rochette, "Mid-infrared sources based on the soliton self-frequency shift," J. Opt. Soc. Am. B **29,** 1347–1355 (2012).
16. A. C. Judge, O. Bang, B. J. Eggleton, B. T. Kuhlmey, E. C. Mägi, R. Pant and C. Martijn de Sterke, "Optimization of the soliton self-frequency shift in a tapered photonic crystal fiber," J. Opt. Soc. Am. B **26,** 2064–2071 (2009).
17. S. Pricking and H. Giessen, "Tailoring the soliton and supercontinuum dynamics by engineering the profile of tapered fibers," Opt. Express **18,** 20151–20163 (2010).
18. R. Pant, A. C. Judge, E. C. Magi, B. T. Kuhlmey, M. De Sterke and B. J. Eggleton, "Characterization and optimization of photonic crystal fibers for enhanced soliton self-frequency shift," J. Opt. Soc. Am. B **27,** 1894–1901 (2010).
19. G. Moltó, M. Arevalillo-Herráez, C. Milián, M. Zacarés, V. Hernández, and A. Ferrando, "Optimization of supercontinuum spectrum using genetic algorithms on service-oriented grids," in *Proceedings of the 3rd Iberian Grid Infrastructure Conference* (IberGrid), 137–147 (2009).
20. A. Ferrando, C. Milián, N. González, G. Moltó, P. Loza, M. Arevalillo-Herráez, M. Zacarés, I. Torres-Gómez and V. Hernández, "Designing supercontinuum spectra using Grid technology," Proc. SPIE **7839,** 78390W (2010).
21. N. Akhmediev and M. Karlsson, "Cherenkov radiation emitted by solitons in optical fibers," Phys. Rev. A **51,** 2602–2607 (1995).
22. J. Wang, Y. J. Geng, B. Guo, T. Klima, B. N. Lal, J. T Willerson and W. Casscells, "Near-infrared spectroscopic characterization of human advanced atherosclerotic plaques," J. Am. Coll. Cardiol. **39,** 1305-1313 (2002).
23. Y. M. Wang, J. S. Nelson, Z. P. Chen, B. J. Reiser, R. S Chuck and R. S. Windeler,"Optimal wavelength for ultrahigh-resolution optical coherence tomography," Opt. Express **11,** 1411-1417 (2003).
24. G, Humbert, W. J. Wadsworth, S. G. Leon-Saval, J. C. Knight, T. A. Birks, P. St. J. Russell, M. J. Lederer, D. Kopf K. Wiesauer, E. I. Breuer and D. Stifter, "Supercontinuum generation system for optical coherence tomography based on tapered photonic crystal fibre," Opt. Express **14,** 1596-1603 (2006).
25. Y. Wang, Y. Zhao, J. S. Nelson, Z. Chen, R. S. Windeler, "Ultrahigh-resolution optical coherence tomography by broadband continuum generation from a photonic crystal fiber," Opt. Lett. **28,** 182–184 (2003).
26. F. Spoeler, S. Kray, P. Grychtol, B. Hermes, J. Bornemann, M. Foerst and H. Kurz, "Simultaneous dual-band ultra-high resolution optical coherence tomography," Opt. Express **15,** 10832-10841 (2007).
27. A.M. Smith, M.C. Mancini, and S. Nie, "Bioimaging: Second window for in vivo imaging," Nat. Nanotechnol. **4,** 710-711 (2009).
28. J.M. Huntley, T. Widjanarko, and P.D. Ruiz, "Hyperspectral interferometry for single-shot absolute measurement of two-dimensional optical path distributions," Meas. Sci. Technol. **21,** 075304 (2010).
29. Q. Cao, N.G. Zhegalova, S.T. Wang, W.J. Akers, and M.Y. Berezin, "Multispectral imaging in the extended near-infrared window based on endogenous chromophores," J. Biomed. Opt. **18,** 101318–101318 (2013).
30. Y. Kodama and A. Hasegawa, "Nonlinear Pulse Propagation in a Monomode Dielectric Guide," IEEE J. Quantum Elect. **23,** 510-524 (1987).
31. R. Driben, B. A. Malomed, A. V. Yulin and D. V. Skryabin, "Newton's cradles in optics: From *N*-soliton fission to soliton chains," Phys. Rev. A **87,** 063808 (2013).
32. S. N. Sivanandam and S. N. Deepa, *Introduction to Genetic Algorithms* (Springer, 2010).
33. F. I. Feldchtein, G. V. Gelikonov, V. M. Gelikonov, R. R. Iksanov, R. V. Kuranov, A. M. Sergeev, N. D. Gladkova, M. N. Ourutina, J. A.Warren, and D. H. Reitze, "In vivo OCT imaging of hard and soft tissue of the oral cavity," Opt. Express **3,** 239?250 (1998).
34. V. M. Gelikonov, G. V. Gelikonov, and F. I. Feldchtein, "Two-wavelength optical coherence tomography," Radiophys. Quantum Electron. **47,** 848?859 (2004).
35. J.G. Fujimoto, C. Pitris, S. A. Boppart and M.E, Brezinski, "Optical coherence tomography: An emerging technology for biomedical imaging and optical biopsy," Neoplasia **2,** 9-25 (2000).
36. J. G. Fujimoto, "Optical coherence tomography for ultrahigh resolution in vivo imaging," Nat. Biotechnol. **21,** 1361–1367 (2003).
37. E. Kerrinckx, L. Bigot, M. Douay and Y. Quiquempois, "Photonic crystal fiber design by means of a genetic algorithm," Opt. Express, **12,** 1990–1995 (2004).

38. W. Q. Zhang, J. E. Sharping, R. T. White, T. M. Monro and S. Afshar V., "Design and optimization of fiber optical parametric oscillators for femtosecond pulse generation," Opt. Express **18,** 17294–17305 (2010).
39. W. Q. Zhang, S. Afshar V. and T. M. Monro, "A genetic algorithm based approach to fiber design for high coherence and large bandwidth supercontinuum generation," Opt. Express **17,** 19311–19327 (2009).
40. R. R. Musin and A. M. Zheltikov, "Designing dispersion-compensating photonic-crystal fibers using a genetic algorithm," Opt. Commun. **281,** 567–572 (2008).
41. Y. Guo-Bing, L. Shu-Guang, L. Shuo and W. Xiao-Yan, " The Optimization of Dispersion Properties of Photonic Crystal Fibers Using a Real-Coded Genetic Algorithm," Chinese Phys. Lett. **28,** 064215 (2011).
42. G. P. Agrawal, *Nonlinear Fiber Optics, 4th ed.* (Academic Press. 2007).
43. S. Afshar V. and T. M. Monro, "A full vectorial model for pulse propagation in emerging waveguides with subwavelength structures part I: Kerr nonlinearity," Opt. Express **17,** 2298–2318 (2009).
44. R. H. Stolen, J. P. Gordon, W. J. Tomlinson and H. A. Haus, "Raman response function of silica-core fibers," J. Opt. Soc. Am. B **6,** 1159–1166 (1989).
45. R. B. Agrawal and K. Deb, *Simulated Binary Crossover for Continuous Search Space* (Technical report, 1994).
46. K. Deb, *Multi-Objective Optimization using Evolutionary Algorithms* (Wiley & Sons, 2001).
47. A.N. Bashkatov1, E.A. Genina, V.I. Kochubey, and V.V. Tuchin, "Optical properties of human skin, subcutaneous and mucous tissues in the wavelength range from 400 to 2000 nm," J. Phys. D: Appl. Phys. **38,** 25432555 (2005).
48. R. Tripathi, N. Nassif, J. S. Nelson, B. H. Park and J. F. de Boer, "Spectral shaping for non-Gaussian source spectra in optical coherence tomography," Opt. Lett. **27,** 406–408 (2002).
49. J. A. Izatt and M. A. Choma, *Optical Coherence Tomography Technology and Applications* (Springer, 2008).

1. Introduction

The Soliton self-frequency shift (SSFS) [1, 2] plays a central role in many effects taking place during supercontinuum (SC) generation in optical fibers (see Refs. [3, 4] for a review on the topic). To mention only a few examples, light trapping [5], multi-peak soliton states [6–8], emission of Airy waves [9], intense dark-soliton SC [10] or broad and intense blue shifted polychromatic dispersive waves [11, 12], would not be possible (or strong enough) without the SSFS. One of the most notorious feature of the Raman effect in SC generation with femtosecond pulses corresponds to the Raman soliton carrying the lowest frequency. Its large frequency shift from the laser pulse has motivated infra-red (IR) Raman soliton sources [13–15] and their optimization [16–20].

In the previous work of Ref. [12], we have shown that fs-pulses traveling in a dispersion engineered single mode fiber (SMF) can generate several pre-defined spectral peaks in the normal group velocity dispersion (GVD) region. These peaks correspond to the narrow band Cherenkov radiation emitted by the bright solitons [21] undergoing Raman red-shift and recoil. Such spectra were important for applications in optical coherence tomography (OCT) with wavelengths in the near infra-red (NIR) window [22–24]: $\lambda \lesssim 1\ \mu$m.

In the present work, we are interested in OCT applications enabled by fiber based illumination [25,26] in the second near IR window (NIR II) [27–29] where $\lambda \in [1, 1.4]\ \mu$m, typically in the anomalous GVD regime of highly nonlinear photonic crystal fibers (PCFs). Because of the typical dispersion landscape, sources in the NIR II window may be based on the bright optical solitons arising during SC generation through the intricate soliton fission effect [30, 31]. With this picture in mind, we used an efficient and general computational optimization method based on genetic algorithms (GA) [32] that is capable of finding output spectra [see Fig. 1] exhibiting two peaks centered at pre-defined wavelengths. This type of multi-peak spectral illumination is very often required for OCT applications in the NIR II [29] and the simultaneous presence of the two operating spectral components is a prerequisite for real time imaging [33, 34]. The two peaks we obtain are the first and second Raman solitons presenting a clean bell-shaped spectral profile, essential for OCT [35], with widths providing a decent longitudinal resolution $l_c \approx 10\ \mu$m [36]. To demonstrate the usefulness of this method, we consider in this work the two spectral channels separated by 100 nm (see, e.g., Ref. [29]). The optimization method finds the optimal input pulse parameters, namely central wavelength, λ_0, temporal width, T_0, and peak power, P_0, yielding the desired spectra. The obtained peak powers are of up to 90 mW

for each spectral band, satisfying the needs for OCT imaging applications [35]. We find by this method the possibility to tune the wavelength of the target spectral channels, what represents an important feature of this strategy since the greatest potential of the given PCF is exploited, specially in situations where limited choice of PCF designs is available.

It is worth mentioning that the use of GAs in optics has indeed proofed useful previously in solving satisfactorily the inverse optimization problem of the one we present here, i.e., the design of PCFs to control SC dynamics, in a wide range of situations [37–41]. The use of GAs generally requires a large amount of simulations. For this reason we used a distributed computing (Grid) platform to reduce the time required to find the optimal solutions. The advantage of this infrastructure is that it enables the use of the same code in a platform of scalable resources which are adapted according to the needs of the particular problem.

2. Supercontinuum modeling and the Genetic Algorithm

We simulate the nonlinear propagation of the complex electric field envelope, A, along the fiber axis, z, by integrating numerically (with split-step fourier method) the generalized nonlinear Schrödinger equation (GNLSE) [42],

$$-i\partial_z A(z,t) = \sum_{q\geq 2} \frac{\beta_q(\omega_0)}{q!}[i\partial_t]^q A(z,t) + \gamma A(z,t)\int_{-\infty}^{+\infty} dt' R(t')|A(z,t-t')|^2, \tag{1}$$

where the β_q's (up to q=10 in this work) account for the linear fiber dispersion and

$$\gamma = \frac{\varepsilon\varepsilon_0^2\omega_0 c}{3}\frac{\int\int dxdy n_2(x,y)[2|\vec{E}|^4+|\vec{E}^2|^2]}{[\int\int dxdy Re\{\vec{E}\times\vec{H}^*\}\hat{u}_z]^2}, \tag{2}$$

is the nonlinearity parameter [43] which has been computed with a FEM solver (comsol) by integrating the electromagnetic components of the modal field at $\lambda = 800$ nm along the transverse fiber cross section: $\gamma \approx 0.07$ /W/m. $\varepsilon = 2.09$ and $n_2 = 2.6\times10^{-20}$ m^2/W are the relative permittivity and nonlinear index of silica glass, respectively. The nonlinear response of the glass is $R(t) = [1-f_R]\delta(t) + f_R h_R(t)$ [44], where $\delta(t)$ is the Dirac delta function and the Raman (delayed) contribution is weighted with $f_R = 0.18$ and described by the damped oscillator

$$h_R(t) = \frac{\tau_1^2+\tau_2^2}{\tau_1\tau_2^2}\Theta(t)\mathrm{e}^{-\frac{t}{\tau_2}}\sin\left(\frac{t}{\tau_1}\right), \tag{3}$$

where $\tau_1 = 12.2$ fs, $\tau_2 = 32$ fs, and $\Theta(t)$ is the Heaviside step function. The input pulses used in our simulations are of the form $\sqrt{P_0}\,\mathrm{sech}(t/T_0)$, where (for a fixed λ_0) the input peak power controls the soliton order $N \equiv T_0\sqrt{\gamma P_0/|\beta_2|}$.

We consider a length $L = 25$ cm of the NL-2.4-800 PCF, exhibiting the lowest zero GVD at 798 nm [see details in Fig. 1], convenient for broad band SC generation with Ti:Sapphire lasers. The frequency conversion performance is investigated within the attainable ranges of input pulse parameters: $\lambda \in [750,850]$ nm, $P \in [5,15]$ kW, and $T \in [30,150]$ fs. For each simulation along the PCF, the GA generates an *individual* with the *genome* $\mid g\rangle \equiv [g_1,g_2,g_3]^T = [T_0,\lambda_0,P_0]^T$ and evaluates how suitable that individual is from the simulation output through the *fitness* function (to be minimized) defined as

$$\phi \equiv \psi_1^{-1}\cdot\psi_2^{-1}, \qquad \psi_j(\omega_{c_j};\Delta\omega) \equiv \int_{\omega_{c_j}-\Delta\omega}^{\omega_{c_j}+\Delta\omega} d\omega' |\tilde{A}(L,\omega')|^2, \qquad j=1,2, \tag{4}$$

where $2\Delta\omega$ is the chosen spectral channel widths and $\omega_{c_j} = 2\pi c/\lambda_{c_j}$ the central frequency. Note that the definition of ϕ as a product tends to favor output spectra in the form $\psi_1 \approx \psi_2$

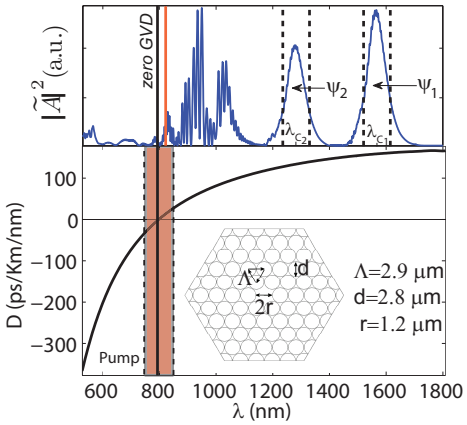

Fig. 1. (Bottom) Dispersion and cross section of the PCF used in our modeling. Shaded area marks the range of the input pump, λ_0. (Top) Typical spectral output and target channels centered at $\lambda_{c_{1,2}}$(delimited by dashed lines) in which $\psi_{1,2}$ are evaluated [See Eq. (4)]. The vertical black line marks the zero GVD and the red one the λ_0 used in this example.

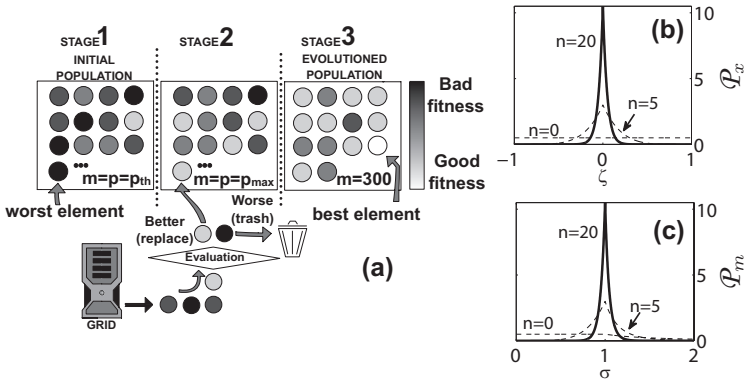

Fig. 2. (a) Sketch of the three GA stages: $p_{th} = 50$, $p_{max} = 100$. Probability distributions for (b) simulated binary crossover (SBX) and (c) polynomial mutation.

amongst all solutions with $\psi_1 + \psi_2 = const$. [see Fig. 3 for optimum results]. The optimization process is depicted in Fig. 2(a). After an initial set of p_{th} randomly (uniformly distributed) generated individuals (stage 1), the genetic operators (GOs) crossover, $\hat{\mathcal{X}}$, and mutation, $\hat{\mathcal{M}}$, are responsible for generating the new *offsprings*, which are added to the population until the maximum size $p = p_{max} > p_{th}$ is reached (stage 2). During stage 3 the population size is kept constant, $p = p_{max}$, and a *replace the worst* strategy is used, i.e., the offspring is added to the population if $\phi_{offspring} < \phi_{max}$ or disregarded otherwise. This steady state GA keeps the Grid constantly computing new individuals in parallel and fully exploits the processing power of the Grid. We briefly describe the GOs below.

Cross-over, $\hat{\mathcal{X}}$, is the first GO applied to the current population and generates two *childs* $|\, g_c^{1,2}\rangle$ by combining two randomly chosen *parents*, $|\, g_p^{1,2}\rangle$, i.e., $\hat{\mathcal{X}}[|\, g_p^1\rangle^T, |\, g_p^2\rangle^T, |\, \emptyset\rangle^T, |\, \emptyset\rangle^T]^T = [|\, g_p^1\rangle^T, |\, g_p^2\rangle^T, |\, g_c^1\rangle^T, |\, g_c^2\rangle^T]^T$ (being $|\, \emptyset\rangle$ the empty set). We have used simulated binary crossover

(SBX) [45] and the $[12\times12]$ operator

$$\hat{\mathcal{X}} \equiv \begin{bmatrix} \hat{I} & \hat{0} & \hat{0} & \hat{0} \\ \hat{0} & \hat{I} & \hat{0} & \hat{0} \\ \hat{\alpha}_+ & \hat{\alpha}_- & \hat{0} & \hat{0} \\ \hat{\alpha}_- & \hat{\alpha}_+ & \hat{0} & \hat{0} \end{bmatrix};\ (\hat{\alpha}_\pm)_{jk} \equiv x_k \frac{1\pm\bar{\sigma}_k}{2}\zeta_{jk},;\ x_k \equiv \Theta(u_k - 0.05), \tag{5}$$

where $\hat{0} \equiv 0\times\hat{I}$ (being $\hat{I}$ the 2×2 identity matrix). The crossover *activators*, x_k, set a probability for cross over of 95% per gene. The stochastic variables in this case, $\bar{\sigma}_k$ [see Fig. 2(b)], are chosen from a uniform random number $u_k \in [0,1]$ according to,

$$\bar{\sigma}_k = \sigma \,/ \int_0^\sigma \mathcal{P}_x(\sigma) = u_k;\ \mathcal{P}_x(\sigma) = \begin{cases} 0.5[n+1]\sigma^n,\ \sigma \le 1 \\ 0.5[n+1]\sigma^{-[n+2]},\ \sigma > 1 \end{cases}. \tag{6}$$

The polynomial mutation, $\hat{\mathcal{M}}$, [46] suitable for real coded problems (continuous valued variables), is applied after $\hat{\mathcal{X}}$ and generates new genes as $\hat{\mathcal{M}} :\mid g\rangle \rightarrow \mid g'\rangle$,

$$g'_k = g_k + m_k \Delta_k \bar{\zeta}_k; \quad m_k \equiv \Theta\left(u_k - \frac{2}{3}\right), \tag{7}$$

where $2\Delta_k$ is the interval size of each variable ($\Delta_\tau = 60$ fs, $\Delta_\lambda = 50$ nm, $\Delta P = 5$ kW). Hence, in average only one gene is mutated per individual when mutation is applied: $\Theta(u_k - 2/3) \Rightarrow P(m_k = 1) = 1/3$. $\bar{\zeta}_k \in [-1,1]$ satisfies the normalized probability distribution [see Fig. 2(c)]

$$\mathcal{P}_m(\zeta) = 0.5\left\{n+1[1-|\zeta|]^n\right\}, \tag{8}$$

with $n = 20$, peaked around $\zeta = 0$ and clearly different from the random generation. For each gene the stochastic variable $\bar{\zeta}$ is chosen from a random $u \in [0,1]$:

$$\bar{\zeta}_k = \zeta / \int_{-1}^{\zeta} \mathcal{P}_m(\zeta) = u_k; \quad u_k \in [0,1]. \tag{9}$$

Statistically, $\hat{\mathcal{M}}$ provides diversity to the population and $\hat{\mathcal{X}}$ explores the parameter space in the vicinity of the parents. In this particular optimization problem, each individual evaluation typically required ~ 90 s what amounted for about 7.5 h of CPU time to perform a single run of the GA with 300 individuals [see Fig. 4]. We used a cluster of 12 cores within a Grid infrastructure, which reduced the computation time to ~ 40 minutes. The Grid protocols supporting the GA execution make infrastructure resizable according to the needs of the problem: number of executions, dimensionality of the search space, etc. (see Ref. [19] for details on the Grid).

3. Dual-pulse solitonic source optimization

As mentioned above, the desired output spectral channels in this work intend to cover OCT applications in the NIR II window, where transparency of the biological tissues increases and scattering decreases [47]. Because spectral bell-shaped pulses avoid spurious structures in OCT images [48], the bright optical solitons are very good candidates for OCT applications. Figure 3 shows the spectral evolutions (bottom) and output spectrograms (top) corresponding to the best individuals obtained by the GA strategy and fitness function, Eq. 4, described in the previous section. All output spectra shown in Fig. 3 present the two reddest solitonic pulses, ejected from the soliton fission, accurately centered in the predefined channels ($\lambda_{c_{1,2}}$) delimited by the dashed lines (see Table I for parameter values associated to results in Fig. 3). In Figs. 3(a) and 3(d), the target spectral channels where chosen from Ref. [29] in order to illustrate the solution for a

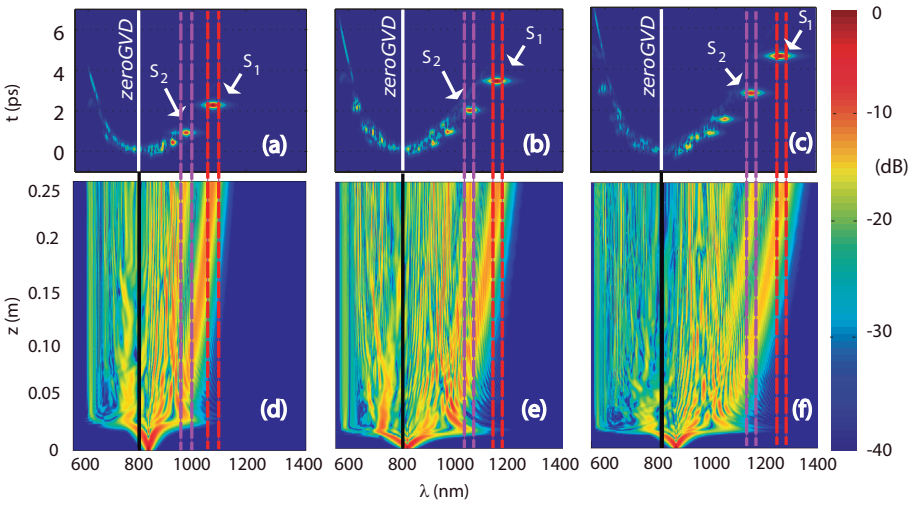

Fig. 3. (a-c) Spectrograms of the output spectra, $z = 25$ cm, corresponding to the optimization results given by the GA algorithm after $m = 300$ evaluations. $S_{1,2}$ label the two solitonic pulses. (d-f) Spectral evolutions along the fiber associated to (a-c), respectively, retrieved from the optimal input pulse parameters corresponding to three different pairs of channels, $\lambda_{c_{1,2}}$. Input pulse parameters are given in Table I. Vertical solid lines mark the zero GVD wavelength.

dual-pulse source required in a realistic application. The other two cases, Figs. 3(b,e) and Figs. 3(c,f), demonstrate the tunability of such source, keeping $\lambda_{c_1} - \lambda_{c_2}$ fixed to 100 nm without replacing the PCF but merely adjusting the input pulse parameters. We checked by benchmarks that several runs of the GA with fixed $\lambda_{c_{1,2}}$ provided systematically very similar optimal results and therefore only one is shown here for each different case.

Regarding OCT applications, another important aspect of the source presented here is that the fs-SC dynamics typically exhibits a very high coherence and negligible shot-to-shot fluctuations [3], known to be detrimental for OCT [35]. Moreover, the two output solitonic pulses ($S_{1,2}$ in Fig. 3) constituting the proposed OCT light source, provide a decent resolution $l_c \equiv 2\ln 2\lambda_s/[\pi\Delta\lambda_{s,FWHM}]$ [49] of ~ 10 μm for the two solitons, $S_{1,2}$.

Table 1. Parameters associated to the best individuals found by the GA, shown in Fig. 3.

Optimal pulse parameters				Spectral bands	Resolution	Fitness	Shown in
T_0 (fs)	λ_0 (nm)	P_0 (kW)	N	$\lambda c_1, \lambda c_2$ (nm)	l_{c_1}, l_{c_2} (μm)	ϕ ($10^{-4}/W$)	
90.01	834.98	5.012	20.14	1075, 975	9.8, 9.5	1.138	Figs. 3(a,d)
70.80	817.27	12.3501	36.24	1150, 1050	10.6, 9.2	1.107	Figs. 3(b,e)
101.13	849.24	9.6617	26.43	1225, 1125	10.1, 10.1	1.018	Figs. 3(c,f)

Figure 4(a) shows the 3D chart in the parameter space containing all 300 individuals involved in the optimization process. Data points distributed all over the volume are typically generated by the random stage 1 ($m < p_{th} = 50$) and GOs tend to accumulate solutions around small volumes where fitness is typically small, with the overall effect of monotonically decreasing the average fitness value, observed when fitness is represented in order of execution [black

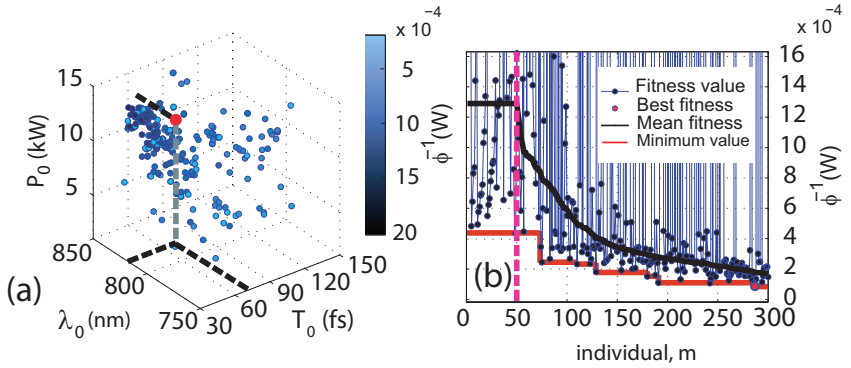

Fig. 4. (a) Parameter space cloud of the 300 individuals (and fitness) generated by the GA in the optimization yielding to the solution in Figs. 3 (b),(e). The best individual is marked in red and dashed mark its input parameters. (b) Fitness evolution versus generated individuals in chronological order. Dashed vertical line marks the threshold population $p_{th} = 50$ corresponding to the end of stage 1 (random generation). Best (at $m \approx 260$), Instantaneous minimum, and average fitness are also plotted (see legend).

curve in Fig. 4(b)]. However, the scattering ability of GOs often results in finding slightly better individuals in nearby regions presenting smaller agglomeration. An important reason for the convergence of our GA towards the optimal solutions is the fact that the operator $\hat{\mathcal{M}}$ is given a lower probability of action than $\hat{\mathcal{X}}$ (probabilities are $1/3$ and 0.95 respectively, see previous section). This combination gives both a good diversity and probability to conserve the properties of the best individuals during the execution of the GA.

4. Conclusions

We presented an efficient optimization procedure based on GAs deployed in the Grid platform, providing faster results and potential scalability of the computational resources. The optimization provides the optimum input pulse parameters required to control the SC dynamics in a way that the first two ejected Raman solitons are centered at two pre-defined wavelengths. The results are shown to be of interest for practical OCT applications in the NIR II region where dual frequency, pulsed sources enable in vivo imaging, and avoid spurious results.

Acknowledgments

F.R.A.S. thanks the Consejo Nacional de Ciencia y Tecnología (CONACyT). F.R.A.S. and M.T.C. acknowledge partial funding provided by the projects CONCyTEG (GTO-2012-C03-195247) and DAIP-UG 382/2014. I.T.G. acknowledges CONACyT for partial support, project: 106764 (CB-2008-1). The work of A.F. was supported by the MINECO under Grant No. TEC2010-15327. C.M. thanks Dr. Miguel Arevalillo Herráez for details on GAs. F.R.A.S thanks Dr. Daniel Ceballos for providing the numerical data for the fiber dispersion.